Pore distances of particulate organic matter predict N 2 O emissions from intact soil at moist conditions

Patricia Ortega-Ramírez, Valérie Pot, Patricia Laville, Steffen Schlüter, David Arturo Amor-Quiroz, Dalila Hadjar, Arnaud Mazurier, Marine Lacoste, Chloé Caurel, Valérie Pouteau, et al.

Geoderma 429 (2023) 116224

Contents lists available at ScienceDirect

Geoderma

journal homepage: www.elsevier.com/locate/geoderma

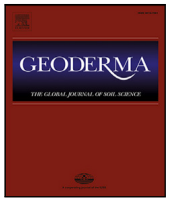

Pore distances of particulate organic matter predict N_2O emissions from intact soil at moist conditions

Patricia Ortega-Ramírez [a,*], Valérie Pot [a], Patricia Laville [a], Steffen Schlüter [b], David Arturo Amor-Quiroz [g], Dalila Hadjar [a], Arnaud Mazurier [c], Marine Lacoste [f], Chloé Caurel [e], Valérie Pouteau [a], Claire Chenu [a], Isabelle Basile-Doelsch [d], Catherine Henault [e], Patricia Garnier [a]

[a] Université Paris-Saclay, INRAE, AgroParisTech, UMR ECOSYS, Thiverval-Grignon, France
[b] Helmholtz Centre for Environmental Research - UFZ, Department of Soil System Science, Halle (Saale), Germany
[c] Institut de Chimie des Milieux et Matériaux de Poitiers, CNRS, Université Poitiers, UMR 7285, Poitiers, France
[d] Aix Marseille Univ, CNRS, IRD, INRAE, Coll France, CEREGE, Aix-en-Provence, France
[e] AgroSup Dijon, INRAE, Université Bourgogne Franche-Comté, UMR Agroécologie, Dijon, France
[f] INRAE, URSOLS, 45075, Orléans, France
[g] SoDa, INRIA Saclay, Palaiseau, France

ARTICLE INFO

Handling Editor: Cornelia Rumpel

Keywords:
Image analysis
X-ray micro CT
Soil
Particulate organic matter

ABSTRACT

Denitrification in soils is a very complex phenomenon due to the multiple factors it depends on. Therefore, making accurate predictions has been an elusive task. In this study we measured N_2O emissions daily during 7 days from a set of 20 undisturbed small soil cores that were subsequently scanned using X-ray micro-tomography. Macropores, particulate organic matter (POM) and the mineral matrix were detected based on a locally-adaptive segmentation method. We proposed an indicator based on the morphology of the soil micro-structure to predict the N_2O emissions. The indicator, $Id_{POM\text{-}air}$, relies on the hypothesis that more N_2O will be emitted when POM is occluded in the soil matrix, i.e. is located at large distances from the next air-filled pore, most likely leading to anoxic conditions, favorable to the production of N_2O. We computed $Id_{POM\text{-}air}$ as the average value of the geodesic distances from the surface of every POM to the closest air-filled pore. For each of the 7 days of measurements $Id_{POM\text{-}air}$ showed a linear trend (each day with an $r^2 > 0.75$) with respect to the N_2O emissions, indicating that the spatial distributions of the POM and air-filled pores were key factors to determine the N_2O emissions in our soil cores.

1. Introduction

Planning a strategy to mitigate global warming requires an in-depth understanding of the different mechanisms of greenhouse gas emissions, in particular of N_2O, which is one of the largest greenhouse gases contributor to global warming (Stocker, 2014). The major N_2O emissions come from agricultural soils, tropical forests and the ocean (Houghton et al., 2001, Mosier et al., 1998, Kroeze et al., 1999). In soils, denitrification is considered to be the main source of N_2O emissions (Knowles, 1982), being the result of microbial respiratory processes during which soluble nitrogen oxides are used as an alternative electron acceptor when oxygen is limiting. The general requirements for denitrification are: the presence of a specific microbial community, the presence of organic carbon compounds, the availability of N-oxides and the limiting oxygen conditions (Philippot et al., 2007). The latter is a function of the physical properties of the soil such as moisture and structure. In fact, the interaction between all these properties causes the complex nature of denitrification in soils.

Many studies have tried to understand the factors that affect denitrification. These studies have to take place at a scale as close as possible to microbial habitats where the N_2O is produced (Parkin, 1987). Parry et al. (1999) studied the influence of the pore space structure and organic matter on denitrification in soil clods and measured at local scale in soil thin-sections the distribution of distances. They concluded that the pore space structure is the major factor explaining the difference of mean denitrification emissions between soil clods from pasture and cropped soils. In more recent studies, X-ray micro computed tomography (μCT) was used to understand the emissions of N_2O using information based on 3D reconstructed images of the soil microstructure. Rabot et al. (2015) used μCT images of soil structure at different hydric states, from which they measured different properties such as air-filled pore volume, water saturation and air-phase

* Corresponding author.
E-mail address: Patricia.ortega@exalumno.unam.mx (P. Ortega-Ramírez).

https://doi.org/10.1016/j.geoderma.2022.116224
Received 22 April 2022; Received in revised form 17 August 2022; Accepted 11 October 2022
Available online 17 November 2022

connectivity. They found that when the soil dried out, the reconnection of the air-filled pore network with the atmosphere allowed high N_2O emissions. Using also μCT images, Kravchenko et al. (2017) found that in relatively dry soil POM had higher water content than the bulk soil, allowing anoxic conditions and enhancement of the N_2O production. In order to allow the transfer of N_2O to the atmosphere, they concluded that the presence of large pores (diameter > 35 μm) was a necessary condition for maximizing the production of N_2O. Kravchenko et al. (2018) put forward that effective predictors of N_2O in soils could be the volume fraction of: water filled pores (< 30 μm), air-filled pores (30–90 μm), poorly aerated soil volume; and the volume of POM isolated from the surface. Schlüter et al. (2019) studied artificial hotspots of growing microbial cultures embedded in sand with different water saturations, from which they found that denitrification depends not only on the amount of microbial hot spots, but also on their spatial distribution in the 3D space. Rohe et al. (2021) found that N_2O+N_2 emissions from repacked columns without particulate organic matter could only be predicted well if at least one proxy for oxygen consumption and oxygen supply are considered. The best predictor for oxygen supply turned out to be the image-derived anaerobic soil volume fraction which was based on distances to air-filled pores in the wet soil matrix. All these results confirm the important role of soil microstructure in predicting N_2O emissions from denitrification. However, to better predict denitrification, these studies indicate that POM acts as hotspots of microbial activity and its propensity to turn anoxic depends on the distance to air-filled pores.

Models of N_2O emission at the field scale like NOE (Hénault et al., 2005), Lanscape-DNDC (Haas et al., 2013), or DAYCENT (Parton et al., 1998) should improve their prediction by incorporating factors linked to spatial organization at the microscale in soil structures. In another way, some mechanistic models are able to consider explicitly the soil structure in order to simulate the gas diffusion in the soil structure, like Rappoldt and Crawford (1999), who used fractal approaches; or Laudone et al. (2011), who considered a pore network of micro and macro pores. Rabot et al. (2015) linked the model NOE to a model of gas transport. However, it is difficult to establish a link between such mechanistic models of soil structure, gas transport and the field scale models of N_2O emission. Another way to improve the models would be to add pertinent factors of soil micro organization that could moderate the N_2O fluxes calculated by macroscale models. However finding relevant indicators remains quite challenging.

This research aims to propose an indicator condensing soil microstructure information in a meaningful way in order to facilitate the prediction of N_2O emissions from soil. This indicator is inspired by the general requirements for denitrification to occur (Philippot et al., 2007). Assuming a similar presence of denitrifiers and N-oxides in our samples, denitrification should be controlled by the limiting oxygen conditions. Therefore, our indicator is based on the hypothesis that the further is the POM to air the larger must be the N_2O emission. The study carried out both N_2O emission measurements in undisturbed soil cores and 3D μCT images of these soil cores. Several morphological indicators based on the 3D images of soil microstructure were calculated. Correlations between N_2O emissions and the different indicators showed that the best morphological indicators explaining N_2O emissions is the indicator based on the geodesic distances between particulate organic matter and the air-filled porosity. Although the scope of this paper is not to determine the source mechanisms of N_2O emissions, but to determine how the microstructure of the soil affects its emissions, discrepancies between N_2O emissions and denitrification activity that arise from denitrification completeness and other N_2O forming processes are discussed.

2. Material and methods

2.1. Experimental field

Soil was sampled from a cultivated field subjected to conventional tillage and management (a maximum of 199 ± 25 kg *N* ha^{-1} yr^{-1} of mineral *N* fertilizers were applied) at "La Cage", Versailles, France. The soil is classified by the World Reference Base for Soil Resources (WRB) as a Luvisol, with a silt loam texture (with 271 g kg^{-1} sand, 562 g kg^{-1} silt and 167 g kg^{-1} clay), with a total carbon content of 10.3 ± 1.2 g kg^{-1} and a pH of 7.4. The same soil plot was monitored by Autret et al. (2019) using automatic chambers during 3.3 years including our sampling period. The measurements varied from 1.33 kg ha^{-1} yr^{-1} to 4.24 kg ha^{-1} yr^{-1}. The largest emission peaks of N_2O were mainly produced after fertilizer application in combination with rainfall events, leading to the conclusion that the main source of the measured N_2O was denitrification, and that the soil contains a microbial community capable of denitrification.

2.2. N_2O emission measurements

We sampled 20 cores (five cm diameter and six cm height) in the soil surface layer (0–10 cm). The cores were numbered arbitrarily. The samples were saturated by capillary rise, in the laboratory during 7 days with a solution of ammonium nitrate. This added 150 mg of nitrogen to 1 kg of dry soil (corresponding to 90 kgN/ha) is about half of the maximum of the mineral *N* fertilizers applied in the field site. *N* was indeed provided in a sufficient large amount so that denitrification was not limited by absence of N.

Then, the samples were equilibrated at a water matric potential of −3.16 kPa using a pressure plate, in order to have optimal conditions for denitrification. Given the size of the water filled pore space of our samples (higher than 60%), most of our emissions must be due to denitrification. The soil cores were then placed in a measurement chamber at a constant temperature of T = 15 °C for 7 days. The soil moisture was monitored during the incubation. It was adjusted by additional NH_4NO_3 solution if necessary to keep a constant moisture value.

The N_2O emitted per day by each soil core were measured with a continuous infrared spectrometer measurement device called IMNOA (Integrated Mesocosms for N_2O Assessments). It measured the gas flow by the connected chamber method (open cell). The installation system allowed to measure the 20 samples in a row. The gas concentrations were monitored continuously with a scan rate of one second, using an infrared spectrometer QCLTILDAS (Aerodyne Research). Mixing ratio of the N_2O was corrected on water vapor dilution and on broadening effects (Harazono et al., 2015; Deng et al., 2017). The duration of the measurement for each cell was 10 min. A full description of our measurement process can be found in Laville et al. (2019).

2.3. X-ray CT images acquisition

After the N_2O measurements, the soil samples were scanned at the University of Poitiers, with an X-ray μCT (EasyTom XL duo, RX Solutions) at the same matric potential of −3.16 kPa. The microtomographic acquisition was done in staking mode with 4320 projections distributed over three turns to scan the whole specimen, starting and ending respectively with the top and bottom of the column in the center of the field of view to reduce artifacts related to the beam conicity. A micro-focus source (Hamamatsu L12161) set at 120 kV and 140 μA was used, coupled to a flat panel detector (Varian PaxScan 2520 DX; 1920 × 1536 matrix pixel; pixel pitch of 127 μm; 16 bits of dynamics) with frame rate of 12.5 fps and an average of 20 images (i.e. total exposure time of 1.6 s). An aluminum filter of 1.2 mm thickness was used to reduce beam hardening effects. The reconstruction was done with the XAct 10251 v1.1 (Rx-Solutions) software package with a filtered back projection algorithm (Feldkamp method-cone beam geometry with Tukey filter and a sinus apodization filter). The result is a set of 16-bit cross sections with a voxel resolution of 32 μm.

2.4. Particulate organic matter size fractionation

After scanning, we randomly selected 10 soil cores out of the 20 samples to measure the amount of POM and total organic carbon. POM is defined as solid fragments of organic matter of size larger than 50 μm (Besnard et al., 1996). Therefore, we applied a particle-size fractionation of organic matter based on mechanical dispersion (disaggregation of soil aggregates in water with glass beads) of the soil as described by Balesdent et al. (1991). The purpose of this separation is to isolate organic residues larger than 50 μm from finer organic matter, dense mineral fractions and organo-mineral associations, by sieving under water and density separation in water. To do so, the cores were manually disrupted and homogenized to recover 50 g aliquot of soil (out of the ≈ 180 g of each soil core). The 50 g of soil were suspended in 180 ml of deionized water with 10 glass beads. The aggregates ruptured by mechanical shaking overnight. Then, the light particulate organic matter was separated from the heavier minerals by flotation sedimentation in water. Coarse fractions > 50 μm were oven dried at 40 °C, while the < 50 μm fraction was freeze-dried. For the carbon content, the fractions were ground in a mortar with a pestle and then sieved to 0.2 mm to ensure homogeneity. The organic carbon content was measured by a CHN elemental analyzer (Vario Isotope Select, 15171064, Germany). This process gave us the corresponding mass and carbon content of each POM fraction.

2.5. Image processing and analysis

The workflow of the image processing and segmentation of the 3D reconstructed soil images is shown in Fig. 1. We first selected a region of interest (ROI) from the raw images of $1753 \times 1753 \times 1700 \sim 5.2 \times 10^9$ voxels obtained after reconstruction. In our case, we selected the cylinder inscribed inside the soil cores, with an average ROI volume of 118 cm^3 (Fig. 1a). This selection was done in Fiji/ImageJ Schindelin et al. (2012) with the "set oval" and "clear outside" functions .

Afterwards, we applied different pre-processing steps to the raw images before their segmentation (Fig. 1b), following the recommendations given in Schlüter et al. (2014). A non-local means filter (Buades et al., 2011) as implemented in the Biomedgroup plugin of Fiji/imageJ was employed for noise removal. The parameters of such plugin were set to: a variance of the noise sigma = 15 and a smoothing factor of 1. Additionally, an edge enhancement unsharp mask filter of radius = 1 was used to reduce partial volume effects due to image blurring where the strength of the filter mask was set to 0.6. Finally, we corrected radial drifts using the software toolbox QuantIm (Vogel et al., 2010) with a method inspired by Iassonov and Tuller (2010).

We expect that, at the voxel resolution of 32 μm in our undisturbed soil samples, we will be able to assign the gray level of each image voxel to one of the different soil constituents: air, water, POM and minerals. Given that water and POM have a similar density, the X-ray attenuation through these materials results in a similar gray level. Schlüter et al. (2014) showed that, when dealing with a multiphase 3D image which has been previously denoised and edge-enhanced, the local multiclass segmentation based on a watershed algorithm succeeds in correctly detecting thin macropores and in avoiding misclassification of boundary voxels into false organic matter coatings around macropores attributed to incorrect assignment of partial volume voxels. Thus, we decided to carry out the watershed segmentation algorithm to identify four classes: air, POM+water, soil matrix and minerals. The soil matrix contains a mixture of air, water, organic matter and minerals or organo-mineral associations of a size smaller than the voxel resolution.

To perform this local segmentation we applied the Marker-controlled Watershed method as implemented in the MorphoLibJ plugin (Legland et al., 2016) in Fiji, which is based on the algorithm of Beucher and Meyer (1990). This plugin requires as input images, the gradient and a global segmentation in both cases of the gray scale image. To create the global segmented image we used the Otsu method

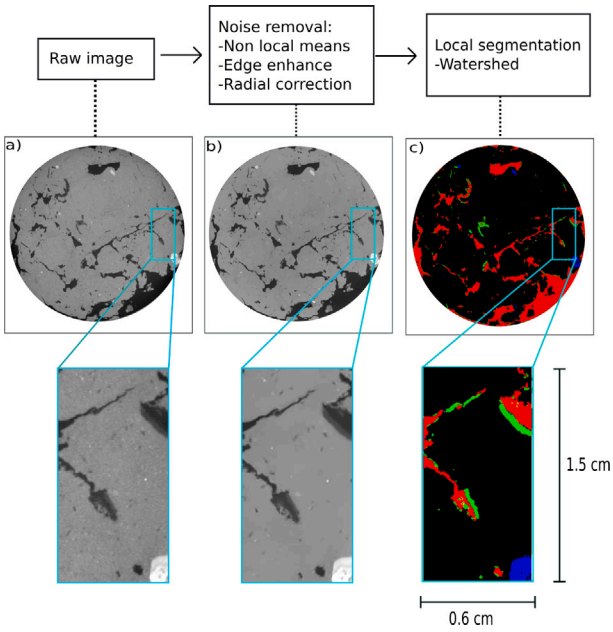

Fig. 1. Image processing work flow example with a 2D slice of an X-ray scan: (a) raw image of the ROI, (b) reduction of noise with non local means filter, edge enhancement and radial correction (c) local segmentation with watershed algorithm. In (a) and (b) the darker is the color the lighter is the material in (c) air in red, POM+water in green, soil matrix in black, and minerals in blue.

(Otsu, 1979) with three thresholds computed with the software toolbox QuantIm (Vogel et al., 2010). While the gradient was obtained with the Fiji function of the same name.

To reduce the noise produced during the segmentation step, a majority filter for a cubic kernel of $3 \times 3 \times 3$ voxels was applied, using the software toolbox QuantIm (Schlüter et al., 2014). This filter action consists in replacing the current label by the most representative label among all neighbors in a cubic kernel.

2.6. Computation of morphological properties

2.6.1. Volume fraction

Following the premise that the reduced oxygen supply to POM should increase N_2O emission from POM, we paid a special attention to correctly distinguish air, water and POM in the segmented images. However, as mentioned above, we could not distinguish water from POM in the POM+water class. Since the soil cores were scanned at a matric potential of −3.16 kPa, we used the Young–Laplace law equation (Eq. (1)) to estimate an equivalent radius that could correspond to radius of water-filled pores due to capillarity.

$$r_{eq} = \frac{2\gamma \cos\theta}{P}. \quad (1)$$

Assuming that water is fully wetting so that the contact angle at the air–water–solid interface is $\theta = 0°$, for an interfacial tension γ of water of 0.075 Nm^{-1}, and P the absolute value of the matric potential, the resulting equivalent radius is r_{eq} = 47 μm, which corresponds to 1.5 voxels of the 3D images. We subsequently assumed that voxels of the POM+water class whose size is smaller than r_{eq} are filled with water. However, taking into account that r_{eq} is close to the resolution limit, this phase may also contain misallocated voxels due to the partial volume effect. The rest of the POM+water class voxels will be considered to contain only POM. In doing so, the 3D images are further distinguished into five material classes: air-filled pores, water-filled pores, POM, soil matrix and minerals. The volume fraction of each class was determined by voxel counting.

For the POM class, we proposed as a first approximation a classification of the size of each POM cluster by comparing them to a sphere of equivalent volume and the size of the POM cluster was associated to the diameter of the equivalent sphere. We defined the same classes than the measured one (50-200 μm, 200-2000 μm, > 2000 μm). The POM clusters were identified by the "Particle analyzer" function of the BoneJ plugin of Fiji (Doube, 2021).

2.6.2. Pore size distribution and connectivity of air-filled pores

To assess the role of air-filled pores in the gaseous diffusion of N_2O produced in the soil microbial habitats, we characterized the morphology of these pores by calculating their cumulative pore size distribution (PSD). For each sample, we created a 3D-image with only the air-filled pore class as the foreground and the rest of the classes as the background. To this image we used a 3D morphological opening function applied to the air-filled pore class, with a sphere of radius r as the structuring element. Openings were calculated for different radius values, from 1, 2, …,5, 8, 10, 15 and 20 voxels, corresponding to pore radius between 32 μm to 640 μm (Vogel, 1997). For each structuring element, we counted the number of remaining voxels of the resulting image, which correspond to air-filled pores larger than the diameter of the structuring element. The opening functions were calculated with the MorholibJ plugin of Fiji (Legland et al., 2016).

To compare the connectivity of the air phase within each soil core, we calculated the size of the largest cluster of air-filled pores using the "Particle Analyzer" function of the BoneJ plugin of Fiji.

2.6.3. Geodesic distance between POM and air-filled pores

In order to understand the production of N_2O in the soil microbial habitats, we proposed a spatial microscopic descriptor, $Id_{\text{POM-air}}$, that describes the proximity of POM to air-filled pores. This descriptor is a global measure of the average geodesic distances between the surface of POM and the nearest air-filled pores within each soil core. Only the POM surface was considered assuming that once that the oxygen makes contact with the POM the denitrification process is affected. It is expected that the larger this descriptor is, the greater the denitrification and N_2O emissions will be.

The spatial descriptor $Id_{\text{POM-air}}$ is obtained by first computing the geodesic distances between the voxels belonging to the surface of a POM and the nearest voxel of air. The geodesic distance is the length of the shortest path joining two points while staying inside a determined region (Lantuéjoul and Beucher, 1981). In this case, the assembly of soil matrix and minerals act as the determined region. We named this distance, $GD_{\text{POM-air}}(i)$, with $i = 1, 2, \ldots, \partial_{POM}$, where ∂_{POM} is the total number of voxels belonging to the surface of POM in all the ROI. Therefore we denoted

$$SGD_{\text{POM-air}} = \sum_{i=1}^{\partial_{POM}} GD_{\text{POM-air}}\,(i)\,, \tag{2}$$

to the sum of geodesic distances (SGD) from every voxel on the surface of every POM in a soil core. We then defined the spatial descriptor as

$$Id_{\text{POM-air}} = \frac{SGD_{\text{POM-air}}}{\partial_{\text{POM}}}\,. \tag{3}$$

$Id_{\text{POM-air}}$ has length units (μm) and it is a way to quantitatively describe the distribution of distances between POM and air-filled porosity.

To compute $GD_{\text{POM-air}}(i)$, we used the function "Interactive Geodesic Distance Map" of the plugin MorphoLibJ of Fiji. This plugin requires two 3D binary images computed from the locally segmented soil image: one with the air and the other with the POM as the foreground. The background of each image is the assembly of the respective remaining materials. From these images, we computed the GDM.

Fig. 2 illustrates the calculation of the geodesic distances between the surface of the POM clusters and the nearest air-filled pore, i.e., the $GD_{POM-air}$ used to calculate $Id_{\text{POM-air}}$ (Eq. (3), and (2)). Figs. 2b and 2c show the air and POM foreground images extracted from the locally segmented images from which the GDM (Fig. 2d) is computed. GDM consists of a color scale image the darker the color of the voxel, the shorter is the distance to an air voxel (for instance we can verify how the darker areas in Fig. 2d correspond to the areas where the air voxels are located in Fig. 2b.). The histogram of $GD_{\text{POM-air}}(i)$ for each column follows approximately a χ^2 distribution, as distances are non-negative (Fig. 2e). The $Id_{\text{POM-air}}$ per column then corresponds to the mean value of the $GD_{\text{POM-air}}(i)$ distribution, as defined in Eq. (3). As a matter of fact, the distribution is not Gaussian and therefore using the normal standard deviation around the mean is not informative, as it would lead to apparently-possible negative distances. Instead, the associated uncertainty is provided by one χ^2-standard deviation understood as the square root of the second central moment, which in such a distribution corresponds to the square root of twice the mean.

The $Id_{\text{POM-air}}$ descriptor is a global measure of the shortest distance of all the voxels belonging to the surface of POM objects to the closer air-filled pore. Therefore, it does not distinguish the role of large or small POM sizes in the emission of N_2O. To explore the role of POM size in the production of N_2O, we recalculated the same descriptor in the local segmented image where POM and air-filled pores smaller than a spherical structuring element of a radius of 2, 3, 4, and 5 voxels were successively eliminated.

2.7. Statistical treatment

Linear regressions were carried out between explanatory variables retrieved from microstructure analysis and N_2O emissions as response variable. These regressions were carried out for individual days rather than the week averages to check for changes in the predictability of N_2O emissions with time. The strategy we use to compute the uncertainty of the slope in our linear regressions is a 5-fold cross-validation. The method consists of iteratively splitting the data such that 80% of it is used for fitting the model. This means that the 20% of data that is unseen during fitting will be different in each of the five possible iterations.

In the case of an ordinary least squares linear regression, ones end up computing five different pairs (intercept, slope) i.e., one per each set, and each one corresponding to an equally valid model. Such analysis makes the linear regression more robust to outliers while providing an approximation to the distribution of possible coefficients that are compatible with the observed data.

3. Results

3.1. N_2O emissions

Fig. 3 shows the cumulative N_2O emissions during the 7 days of measurements for each soil core. Emissions were variable with no particular trend over time. During the first day a large variation between the samples was observed with an average amount of 48.9 $\mu g_{N_2O}/Kg_{DrySoil(DS)}$ and standard deviation of 42.6 $\mu g_{N_2O}/Kg_{DS}$. Four samples emitted less than 10 $\mu g_{N_2O}/Kg_{DS}$ whereas three samples emitted more than 100 $\mu g_{N_2O}/Kg_{DS}$. Generally, the differences in N_2O emissions between the samples were maintained during the 7 days The ranking from low- to high emitting cores was rather consistent over time. However, in some instances like core 14, there was a proportional drop in N_2O emissions occurring already at the second day.

3.2. Volume fraction and morphological properties of air-filled pores

The volume fraction of the different classes per soil core are given in Fig. 4. On average, the air-filled pores, POM, water-filled pores, soil matrix, and mineral fractions were: 10.74%, 2.56%, 0.46%, 84.56%, and 0.15% with a coefficient of variation of 0.38, 0.23, 0.23, 0.08, and 0.66, respectively. The water-filled pore fraction, computed from the

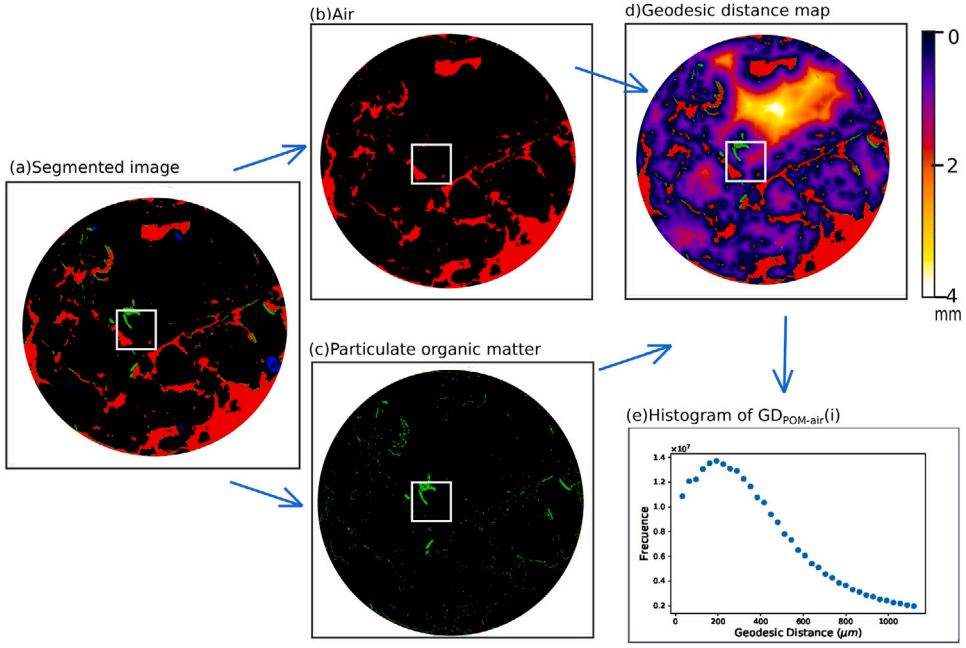

Fig. 2. Workflow of the image analysis process, illustrated with a transverse section of one of our columns. (a) the locally segmented image (air in red, POM in green, soil matrix in black, and minerals in blue). (b) and (c) have the air and the POM as the foreground respectively. (d) is the GDM of the background of (c) to the air-filled pores in (b). (e) shows the counting number that a $GD_{\text{POM-air}}(i)$ appears on the whole sample. The white square locates a region (9.6 mm × 9.6 mm) that will be displayed in Fig. 12.

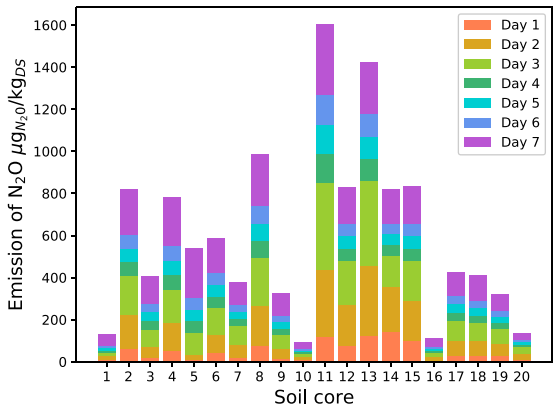

Fig. 3. Cumulative amounts of N_2O emitted per soil core during the 7 days of measurements.

POM+water class (see Section 2.6.1) represented thus 15% of this class fraction.

The cumulative PSD of the air-filled pores varied largely between the soil samples (Fig. 5). For instance, the extreme variations are at a radius of 150 μm are found in core 11 and core 8 where porosity occupied by pores of radius smaller that 150 μm is 20% and 50% respectively. As the radius increases, so does the difference in the cumulative PSD till the maximal radius of 250 μm.

The connectivity of the air phase was high in the soil cores where the largest cluster of air-filled pores consisted, on average, of 88 ± 12% of the total air porosity.

3.3. POM characterization

The experimental POM size fractionation in the ten analyzed soil cores showed an average POM content of 13.4 ± 4.4 mg/g_{DS} partitioned in: 0.4 ± 0.6 mg/g_{DS} (POM>2 mm), 3.2 ± 2.8 mg/g_{DS} (0.2<POM<2 mm), 9.8 ± 5.0 mg/g_{DS} (0.05<POM<0.2 mm). The distribution of POM in our samples was very heterogeneous across the soil cores.

The volume occupied by POM identified in the segmented μCT images of the same ten soil cores, was on average 26.11 ± 4.98 mm^3/cm^3_{soil}. When comparing the size of each cluster of POM to spheres of equivalent volume, and associating the diameter of the sphere to the size of POM, POM was partitioned into 7.86 ± 4.11 mm^3/cm^3_{soil} (POM>2 mm), 17.56 ± 2.45 mm^3/cm^3_{soil} (0.2<POM<2 mm) and 0.66 ± 0.67 mm^3/cm^3_{soil} (0.05<POM<0.2 mm), according to particle analyzer algorithm. The experimental method reports a big proportion of the volume occupied by the smallest fraction (50-200 μm), whereas the computed method reports the opposite.

We fitted a linear regression forcing the intercept to zero[1] (r^2_0 = 0.89) with a slope of 0.81 ± 0.06 g_{POM}/cm^3_{POM} (Fig. 6, which can be associated to the bulk POM density (Kravchenko et al., 2014). The strategy we used to compute the bulk POM density is a 5-fold cross-validation, as mentioned in Section 2.7. The mean slope (solid blue line in Fig. 6) is then interpreted as the expectation value for the density while the uncertainty corresponds to the standard deviation of the set of the 5 cross-validated slopes.

3.4. Understanding the N_2O emissions through soil microstructure

3.4.1. Air-filled porosity and POM

We correlated the accumulated N_2O emissions of each soil core during each of the 7 days of measurements and the air-filled porosity (Fig. 7a shows this correlation with the seventh day as an example). Although the soil cores where the air fraction is higher were the soil cores that emitted less N_2O, the linear dependence was found to be weak for air-filled porosity at each of the 7 days (r^2 <0.52). The variability in N_2O emissions explained by POM volume fraction (Fig. 7b), or carbon content was even weaker (r^2 < 0.30 for the POM

[1] r^2_0 is the coefficient of determination when the intercept is forced to zero). Given the formulas associated to compute r^2_0 and r^2, in this case r^2_0 is higher than r^2) (Eisenhauer, 2003)

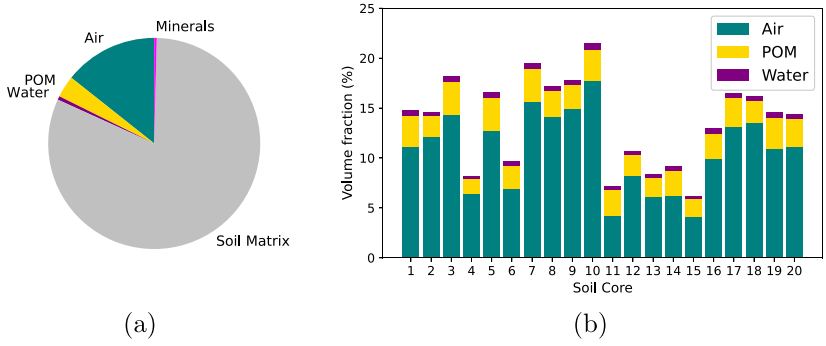

Fig. 4. Volume fraction of the five material classes air-filled pores, POM, water-filled pores, soil matrix, and minerals obtained after watershed segmentation (a) for the case of soil core 3, (b) volume fraction of the air-filled pores, POM and water-filled pores for each soil core. Note that the soil matrix may contain water and POM of size smaller than the voxel resolution of 32 μm.

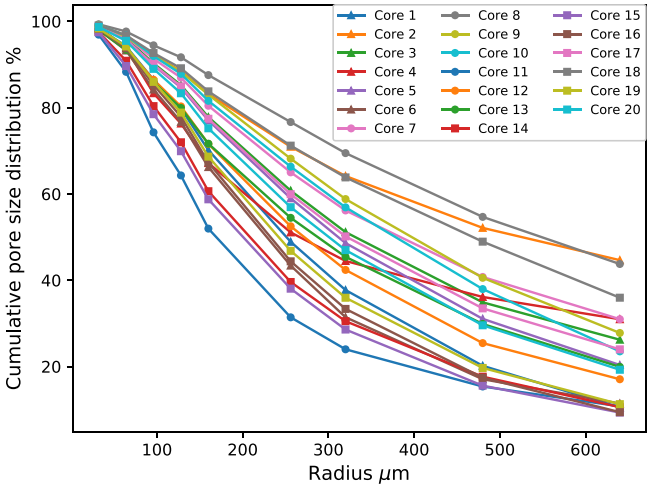

Fig. 5. Cumulative PSD of the air-filled pores computed for radius from 1 voxel till 20 voxels (32 μm to 640 μm).

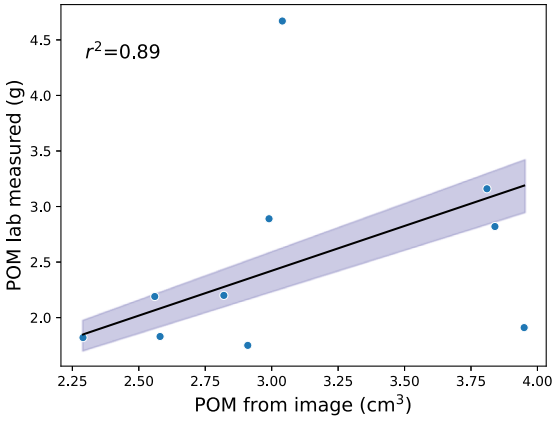

Fig. 6. Comparison of POM mass measured through the laboratory fractionation method and POM volume identified in the segmented μ CT image. The shaded region in blue corresponds to the set of cross-validated linear regressions with intercept forced to zero and slopes ranging in 0.81 ± 0.06 mg/mm^3.

and r^2 < 0.50 for the carbon), irrespective of the investigated day. However, a less expected result is that N_2O emissions were negatively correlated to POM. It might be related to wrongly assigned voxels due to partial volume effects present when the pore area is large. Therefore, a much more successful attempt is proposed in the following section.

3.4.2. N_2O emission function of $Id_{POM\text{-}air}$

The variation of N_2O emissions between the soil samples could therefore be less dependent on how much POM or air porosity is in a sample, but how good is the access of the POM to the air-filled pores. To check this assumption we performed linear regression of daily N_2O emissions with $Id_{\text{POM-air}}$ for the entire week (Fig. 8). We found a positive linear relationship with coefficients of regression r^2 of : 0.75, 0.81, 0.80, 0.80, 0.79 0.79, 0.78 for day 1, day 2, …, day 7 respectively. These values are much higher than the ones found for the other calculated morphological parameters 3.4.1.

3.4.3. The role of POM sizes and air-filled pores

When small air-filled pores and POM are progressively removed (Fig. 9), the GDMs showed larger and larger values of $GD_{\text{POM-air}}(i)$ (keeping the χ^2 distribution shape as in Fig. 2e), as can be seen in Fig. 9a to Fig. 9e there is an increase in the presence of light colors.

Fig. 10 shows the plot of the $Id_{\text{POM-air}_{Ri}}$ (where i = 1,2, …,5) descriptors calculated for each soil core in function of the accumulated N_2O emissions during the seventh day of measurements. During each of the 7 days we noticed the expected increase of the intercept as the radius of the structuring element increases, whereas the regression coefficients r^2 remained similar for all the radius and days (average r^2 = 0.77 ± 0.05).

The χ^2 distribution of $GD_{\text{POM-air}}(i)$ (histogram in Fig. 2e) showed largest frequencies for the small $GD_{\text{POM-air}}(i)$. This result may imply the presence of many small air-filled pores very close to POM, or the presence of many small particles of POM close to air-filled pores. The effect of removing the small air-filled pores and POM decreased the frequency of small $GD_{\text{POM-air}}(i)$ leading to a smaller slopes as the radius increases (Fig. 10).

4. Discussion

4.1. POM detection

It has been proved experimentally that POM plays a crucial role at explaining N_2O production and its variability (Parry et al., 2000; Surey et al., 2021). Individual microbial hotspots formed on particulate organic matter may contribute more to N_2O emissions than the vast volume occupied by mineral-associated organic matter (Parkin, 1987). Therefore, a detailed POM inventory represents an untapped potential for improving N_2O emissions.

The heterogeneous spatial distribution of POM in the 3D soil architecture can be revealed by the use of μCT images. Although easily recognizable shapes of POM can be visually detected, a systematic identification of POM still remains a challenge for segmentation algorithms (Kravchenko et al., 2014; Kravchenko et al., 2018 Maenhout et al., 2021; Schlüter et al., 2022a; Piccoli et al., 2019; Lammel et al., 2019).

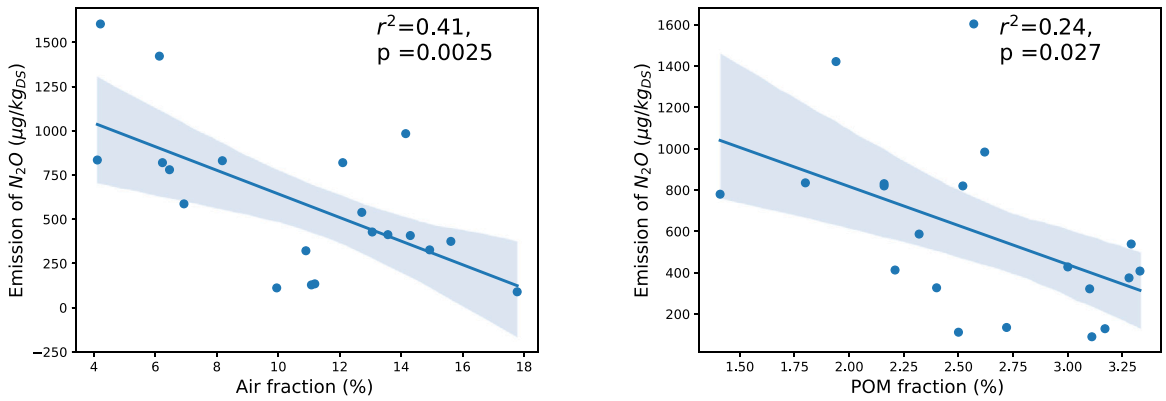

Fig. 7. Air (a) and POM (b) fractions per soil core as a function of the accumulated N_2O emission during the seventh day, with their respective tendency line. The shaded area corresponds to the 95% confidence interval band for the fitted slope and intercept (which implies a 95% chance that the true regression line fits within the confidence bands).

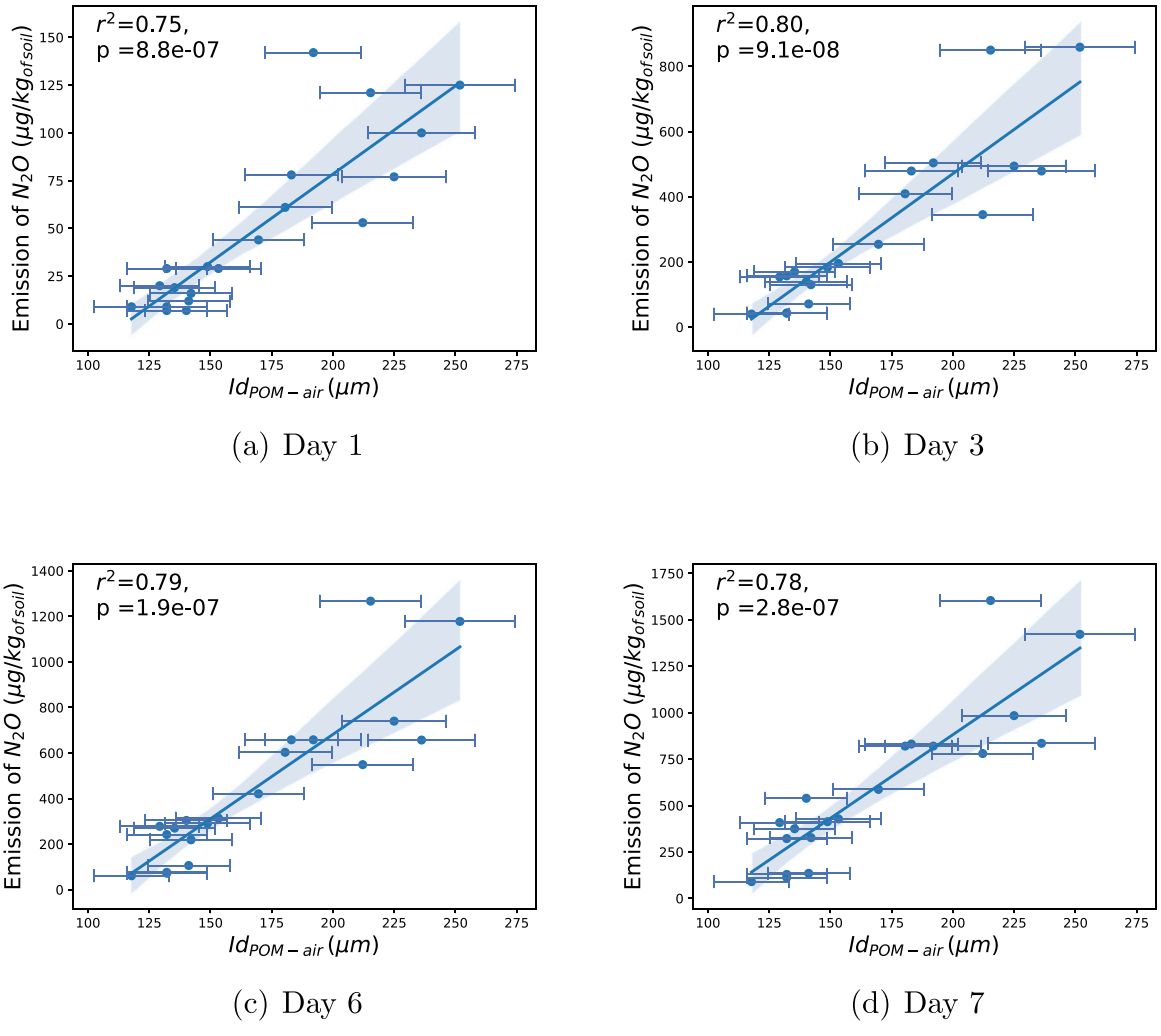

Fig. 8. $Id_{\text{POM-air}}$ as a function of the N_2O emissions measured during 7 days. The blue line is the linear regression fit, along with a translucent 95% confidence interval band. The uncertainty of $Id_{\text{POM-air}}$ (the horizontal bars) is exclusively due to the dispersion in the distribution of distances $GD_{\text{POM-air}}(i)$ in each soil core.

Few studies tried to quantitatively compare POM computed in μCT images and experimental measurements (Kravchenko et al., 2014;Piccoli et al., 2019; Zheng et al., 2020). Similarly to Kravchenko et al. (2014), the comparison of the measured total mass of POM from laboratory measurement and the total volume of POM computed from μCT images indicated a linear relationship. The value of the derived POM bulk density of 0.81 g/cm^3 is somewhat smaller than the value of 0.98 g/cm^3 found in Kravchenko et al. (2014). It is at the lower end of the range of densities of biochemicals (0.8–1.7 g/cm^3) and consistent with the fact that operationally, in the method proposed

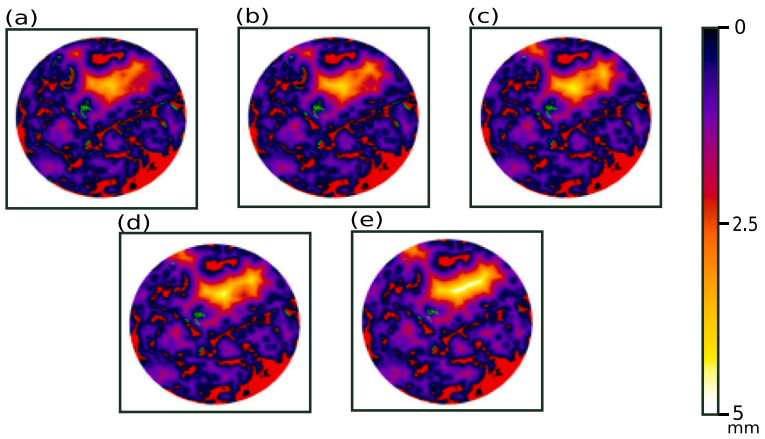

Fig. 9. 2D slice of a soil core to exemplify the evolution of the GDM. In (a) is the GDM of the original image (See Section 3.4.2), (b) to (e) are the GDMs while eliminating POM and air-filled pores of radius = 2, 3, 4, and 5 voxels respectively.

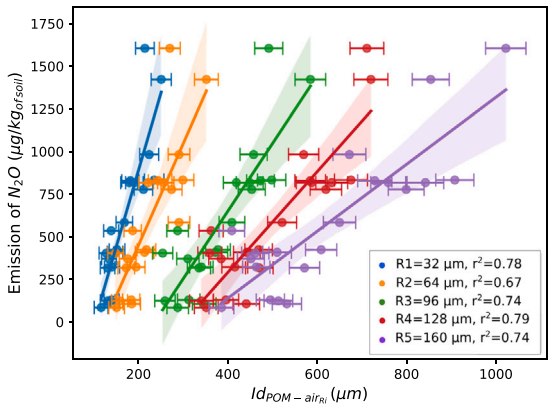

Fig. 10. N_2O emissions at day 7 in function of the descriptors $Id_{\text{POM-air}_{Ri}}$. Each of them present its linear regression along with a translucent 95% confidence interval band.

by Balesdent et al. (1996), POM are separated by flotation in water. However, it is smaller than the density of soil POM, usually considered in the literature to range between 1.20 and 1.64 g/cm^3 in studies where fractionations were carried out with heavier liquids (Chenu and Plante, 2006; Mayer et al., 2004; Leuther et al., 2022).

Additional explanations to the density value that we found, are related to the quality of μCT images and POM segmentation. On the one hand, the low value of POM bulk density can reflect the different stages of decomposition of the plant residues in the soil which form assemblages of different spatial organization and density of organic molecules and voids (Elyeznasni et al., 2012; Kravchenko et al., 2014). Due to too low μCT scan resolution, the gray levels associated with POM objects encompass a lot of void volume leading to artificially low densities. On the other hand, the multi-class segmentation and/or the separation of classes between water and POM may have not prevented all misclassification of voxels. This probably led to a larger POM volume than the real one. We tested the sensitivity of such POM misclassification by systematically removing POM coatings and POM objects smaller than 64 µm diameter by applying a morphological opening on the segmented POM as proposed in Kravchenko et al. (2014). The resulting POM volume was smaller and was linearly related to the mass of POM (r_0^2 = 0.83) with a slope of 1.4 ± 0.2 g/cm^3 and the intercept forced to 0, as we expect the mass to be exactly zero for vanishing volume and vice-versa. This value is within the range of density of organic molecules. This modification to the POM at image analysis level shows how important it is to find accurate methods and establish a standard methodology to identify POM in μCT images. An improved method of POM detection might be a segmentation based on machine-learning that takes gradient and texture information at several spatial scales into account in addition to gray scale information, as it was done in Schlüter et al. (2022a,b). Eventually, the accurate and robust determination of POM volumes and POM densities by microstructure analysis might lead to a better prediction of potential hotspots for microbial activity in soil and render destructive methods unnecessary. In addition, only the image-based POM analysis yields additional information about its position within the pore network.

There was a considerable discrepancy in POM size classes between both methods. This discrepancy comes at no surprise since (1) the effective diameter of fibrous POM cannot be determined from its volume and (2) the mechanical dispersion of soil prior to sieving may have caused a bias towards smaller chunks of POM as compared to its intact state during imaging. Eventually, the size of POM is irrelevant for predicting N_2O emissions, as long as its position within the intact pore network is accounted for.

4.2. N_2O *predictions*

The working hypothesis that the oxygen supply of POM from air-filled pores would be a good predictor of N_2O emissions was confirmed by the incubation results. The oxygen supply was quantitatively described by a single number, the descriptor $Id_{\text{POM-air}}$, calculated at the scale of the soil cores by using the concept of geodesic distances. This descriptor encloses information on the microstructure of the soil via the geodesic distances of POM to the closest air-filled pore.

Other studies have used the concept of geodesic distances to understand denitrification. Rohe et al. (2021) computed geodesic distances in μCT soil images between non-air voxels (except minerals) to the connected air-filled pores, to calculate the anaerobic soil volume fraction. This indicator, combined with measured CO_2 emissions succeeded to predict N_2O emissions. In Rohe et al. (2021) all POM was removed prior to soil packing, which explains why air distances were measured in the entire soil matrix, in which mineral-associated organic matter was distributed homogeneously. In our study within intact soil, large amounts of POM were present, which justified to focus the analysis of air-distances on these microbial hotspots and disregard the contribution of N_2O emissions from the soil matrix. Parry et al. (1999), computed in 2D soil thin-sections the geodesic distances of any point of the soil matrix to air-filled pores. They found a larger average distance in cropped soil clods compared to pasture soil clods where the latter had lower mean denitrification rates. They further concluded that the heterogeneous POM distribution in the cropped soil clods played an important role in the skewed distribution of denitrification. Our descriptor supported this hypothesis.

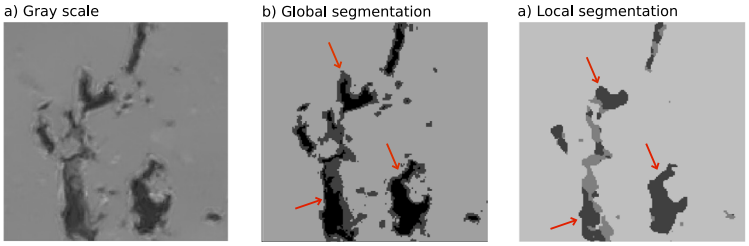

Fig. 11. Selected view of a 2D cross-section of a segmented image showing air, POM+water, soil matrix and minerals. In (a) the raw image after pre-processing filters (the darker is the color the lighter is the material); in (b) the global segmented image; in (c) the local segmented image. In (b) and (c) the colors black, dark gray, light gray and white correspond to air, POM+water, soil matrix, and minerals, respectively. Red arrows indicate locations of false organic coatings in the global segmentation method.

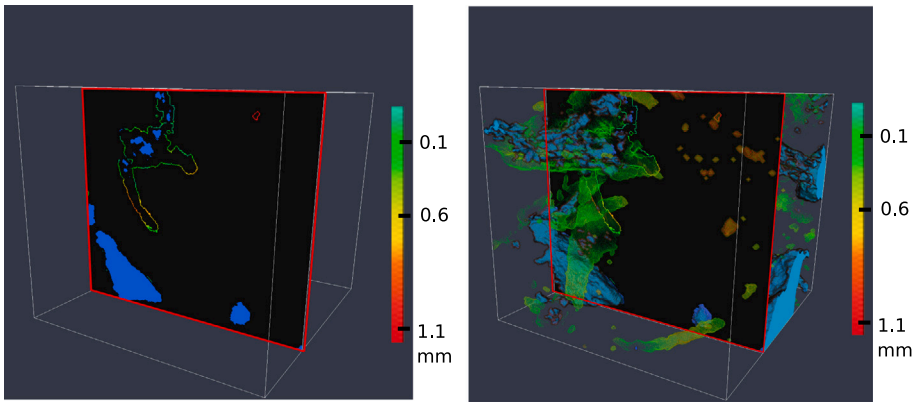

Fig. 12. Zoom to the geodesic distance obtained in 2. In blue are the air-filled pores, and in color scale the surface of the POM. (a) shows a 2D slice, (b) the same region but in 3D.

The $Id_{\text{POM-air}}$ indicator alone largely explained the measured N_2O emissions and was superior to the predictive power of volume fractions of POM and air-filled porosity alone. Similar values of the linear regression coefficients were obtained throughout the 7 days of measurements, indicating the robustness of $Id_{\text{POM-air}}$ as a good indicator of the production of N_2O (Fig. 8). The soil cores with small $Id_{\text{POM-air}}$ were the ones featuring smaller N_2O emissions, confirming that the farther is POM from air, the bigger are the N_2O emissions. When removing successively the small POM and air-filled pore objects, the quality of the linear regression between $Id_{\text{POM-air}}$ and N_2O emissions remained similar (Fig. 10). This indicated that even if the multiclass segmentation may have over classified partial volume voxels into POM, it has a low impact on the linearity of the relation between $Id_{\text{POM-air}}$ and N_2O fluxes. It also implies that it is not the size of the air-filled pores nor that of POM that controlled the N_2O emissions in our experiment, but rather the distribution of distances between these materials independently of their size.

4.3. Limitations

The sole measurement of N_2O emissions without additional isotopic information cannot discriminate between different N_2O formation processes. Likewise, without data on the N_2 production, we lack information to understand whether N_2O emissions are low because it is not formed at all, it is reduced to N_2 before being emitted or it is trapped in disconnected pores. At least the latter process, which was evident at high water saturations in Rohe et al. (2021) can be largely excluded for our intact soil cores with a natural pore network incubated at −3.1 kPa, as the air-filled porosity exhibited high connectivity. Independent N_2O emission data from field monitoring campaigns from were the soil cores were extracted (Autret et al., 2019) strongly suggest that denitrification is the most dominating N_2O formation at this matric potential. Most likely N_2O reduction was not a dominating process at this matric potential and only contributed little to the unexplained variability of N_2O emission, as bulk oxygen supply was still relatively high and only limited locally in microbial hotspots. Therefore, the predictive power of the introduced microstructural parameter on N_2O emissions was very good under these experimental conditions, despite the lack of detailed process understanding.

5. Conclusions

The objective of the present study was to explore the interplay between soil microscopic structure and soil N_2O emissions. We took advantage of the inherent spatial variability of N_2O emissions, particulate organic matter and soil structure at the scale of small cores and implemented an innovative combination of experimental measurement, visualization and image analyses. This led us to the conclusion that it was not the volume fraction of POM and air-filled pores but their spatial distribution that controlled the N_2O emissions of the soil cores. This study on undisturbed soil samples highlights how the distribution of POM with respect to air-filled pores can strongly affect the N_2O emissions of soils. To confirm the robustness of this descriptor we suggest to evaluate it in other pedoclimatic conditions and segmentation methods to identify POM in μCT images.

Declaration of competing interest

The authors declare that they have no known competing financial interests or personal relationships that could have appeared to influence the work reported in this paper.

Data availability

Data will be made available on request.

Acknowledgments

The research described in this article was made possible by the financial support of the ANR, France Project Soil-μ3D (Number ANR-15-CE01-0006-01). Patricia Ortega-Ramírez was funded by the ANR, France project NanoSoilC (Number ANR-16-CE01-0012-03). We acknowledge the PLATeforme INstrumentale d'Analyse (PLATINA) of the IC2MP (University of Poitiers) for access to the micro-CT device. AM acknowledges financial support from the European Union (ERDF) and 'Région Nouvelle Aquitaine', France.

Appendix. Supplementary material

A.1. Segmentation

In this supplementary section we compare the multi-class image obtained after the watershed local segmentation (Fig. 11c) to the raw image (Fig. 11a) and the image segmented by the global Otsu's segmentation method (Fig. 11b). We observed that the global segmentation systematically assigned POM+water class to the voxels bordering air-filled pores, whereas the local segmentation method did not (see red arrows in Figs. 11b and 11c which indicate false organic coatings in the global segmented image).

A.2. 3D visualization of the $GD_{POM-air}$

In Section 2.6.3 is explained how we computed the GDM. In order to improve the comprehension of this concept, Fig. 12 presents a closeup of the red square area drawn in Fig. 2 but embedded in a 3D space. The air-filled pores (previously black in Fig. 2b are now represented in blue; the values of the geodesic distances (earlier shown in gray colors in Fig. 2) are now represented in a palette of colors from red to green, where the redder the color, the greater its geodesic distance; and the remaining voxels which can be soil matrix, minerals, but also interior parts of the POM are now represented in black.

References

Autret, Bénédicte, Beaudoin, Nicolas, Rakotovololona, Lucia, Bertrand, Michel, Grandeau, Gilles, Gréhan, Eric, Ferchaud, Fabien, Mary, Bruno, 2019. Can alternative cropping systems mitigate nitrogen losses and improve GHG balance? Results from a 19-yr experiment in Northern France. Geoderma 342, 20–33.

Balesdent, Jerome, Mariotti, Andre, et al., 1996. Measurement of soil organic matter turnover using 13C natural abundance. Mass Spectrom. Soils 41 (3), 83–111.

Balesdent, Jerome, Pétraud, J.P., Feller, Christian, 1991. Effets des ultrasons sur la distribution granulométrique des matières organiques des sols. Sci. Du Sol 29 (2), 95–106.

Besnard, E, Chenu, C, Balesdent, Jerome, Puget, P, Arrouays, Dominique, 1996. Fate of particulate organic matter in soil aggregates during cultivation. Eur. J. Soil Sci. 47 (4), 495–503.

Beucher, Serge, Meyer, Fernand, 1990. Morphological Segmentation. Academic Press.

Buades, Antoni, Coll, Bartomeu, Morel, Jean-Michel, 2011. Non-local means denoising. Image Process. Line 1, 208–212.

Chenu, Claire, Plante, A.F., 2006. Clay-sized organo-mineral complexes in a cultivation chronosequence: Revisiting the concept of the 'primary organo-mineral complex'. Eur. J. Soil Sci. 57 (4), 596–607.

Deng, Hao, Sun, Juan, Liu, Ningwu, Wang, Hongliang, Yu, Benli, Li, Jingsong, 2017. Impact of H_2O broadening effect on atmospheric CO and N_2O detection near 4.57 μm. J. Mol. Spectrosc. 331, 34–43.

Doube, Michael, 2021. Multithreaded two-pass connected components labelling and particle analysis in image. J. R. Soc. Open Sci. 8 (3), 201784.

Eisenhauer, Joseph G., 2003. Regression through the origin. Teach. Stat. 25 (3), 76–80.

Elyeznasni, Nadia, Sellami, F, Pot, Valérie, Benoit, Pierre, Vieublé-Gonod, L, Young, Iain, Peth, S, 2012. Exploration of soil micromorphology to identify coarse-sized OM assemblages in X-ray CT images of undisturbed cultivated soil cores. Geoderma 179, 38–45.

Haas, Edwin, Klatt, Steffen, Fröhlich, Alexander, Kraft, Philipp, Werner, Christian, Kiese, Ralf, Grote, Rüdiger, Breuer, Lutz, Butterbach-Bahl, Klaus, 2013. LandscapeDNDC: a process model for simulation of biosphere–atmosphere–hydrosphere exchange processes at site and regional scale. Landscape Ecol. 28 (4), 615–636.

Harazono, Yoshinobu, Iwata, Hiroki, Sakabe, Ayaka, Ueyama, Masahito, Takahashi, Kenshi, Nagano, Hirohiko, Nakai, Taro, Kosugi, Yoshiko, 2015. Effects of water vapor dilution on trace gas flux, and practical correction methods. J. Agric. Meteorol. 71 (2), 65–76.

Hénault, Catherine, Bizouard, Florian, Laville, P, Gabrielle, B, Nicoullaud, Bernard, Germon, JC, Cellier, Pierre, 2005. Predicting in situ soil N_2O emission using NOE algorithm and soil database. Global Change Biol. 11 (1), 115–127.

Houghton, John Theodore, Ding, YDJG, Griggs, David J, Noguer, Maria, van der Linden, Paul J, Dai, Xiaosu, Maskell, Kathy, Johnson, CA, 2001. Climate Change 2001: the Scientific Basis. The Press Syndicate of the University of Cambridge.

Iassonov, Pavel, Tuller, Markus, 2010. Application of segmentation for correction of intensity bias in X-ray computed tomography images. Vadose Zone J. 9 (1), 187–191.

Knowles, Roger, 1982. Denitrification. Microbiol. Rev. 46 (1), 43–70.

Kravchenko, Alexandra N, Guber, Andrey K, Quigley, Michelle Y, Koestel, John, Gandhi, Hasand, Ostrom, Nathaniel E, 2018. X-ray computed tomography to predict soil N_2O production via bacterial denitrification and N2O emission in contrasting bioenergy cropping systems. Gcb Bioenergy 10 (11), 894–909.

Kravchenko, A.N., Negassa, Wakene, Guber, A.K., Schmidt, Sonja, 2014. New approach to measure soil particulate organic matter in intact samples using X-ray computed microtomography. Soil Sci. Am. J. 78 (4), 1177–1185.

Kravchenko, AN, Toosi, ER, Guber, AK, Ostrom, NE, Yu, J, Azeem, K, Rivers, ML, Robertson, GP, 2017. Hotspots of soil N_2O emission enhanced through water absorption by plant residue. Nat. Geosci. 10 (7), 496–500.

Kroeze, Carolien, Mosier, Arvin, Bouwman, Lex, 1999. Closing the global N_2O budget: a retrospective analysis 1500–1994. Glob. Biogeochem. Cycles 13 (1), 1–8.

Lammel, Daniel R, Arlt, Tobias, Manke, Ingo, Rillig, Matthias C, 2019. Testing contrast agents to improve micro computerized tomography (μCT) for spatial location of organic matter and biological material in soil. Front. Environ. Sci. 153.

Lantuéjoul, Christian, Beucher, Serge, 1981. On the use of the geodesic metric in image analysis. J. Microsc. 121 (1), 39–49.

Laudone, GM, Matthews, GP, Bird, NRA, Whalley, WR, Cardenas, LM, Gregory, AS, 2011. A model to predict the effects of soil structure on denitrification and N_2O emission. J. Hydrol. 409 (1–2), 283–290.

Laville, Patricia, Fanucci, Olivier, Chandra, Varunesh, 2019. Integrated mesocosms for N_2O emissions and soil carbon storage assessments: validation and qualification of a new laboratory device: IMNOA. In: 2019 IEEE International Workshop on Metrology for Agriculture and Forestry (MetroAgriFor). IEEE, pp. 30–34.

Legland, David, Arganda-Carreras, Ignacio, Andrey, Philippe, 2016. MorphoLibJ: integrated library and plugins for mathematical morphology with ImageJ. Bioinformatics 32 (22), 3532–3534.

Leuther, Frederic, Wolff, Maximilian, Kaiser, Klaus, Schumann, Lena, Merbach, Ines, Mikutta, Robert, Schlüter, Steffen, 2022. Response of subsoil organic matter contents and physical properties to long-term, high-rate farmyard manure application. Eur. J. Soil Sci. e13233.

Maenhout, Peter, De Neve, Stefaan, Wragg, Joanna, Rawlins, Barry, De Pue, Jan, Van Hoorebeke, Luc, Cnudde, Veerle, Sleutel, Steven, 2021. Chemical staining of particulate organic matter for improved contrast in soil X-ray μCT images. Sci. Rep. 11 (1), 1–11.

Mayer, Lawrence M, Schick, Linda L, Hardy, Kathleen R, Wagai, Rota, McCarthy, John, 2004. Organic matter in small mesopores in sediments and soils. Geochim. Cosmoch. Acta 68 (19), 3863–3872.

Mosier, Arvin, Kroeze, Carolien, Nevison, Cindy, Oenema, Oene, Seitzinger, Sybil, Van Cleemput, Oswald, 1998. Closing the global N_2O budget: nitrous oxide emissions through the agricultural nitrogen cycle. Nutr. Cycl. Agroecosyst. 52 (2), 225–248.

Otsu, Nobuyuki, 1979. A threshold selection method from gray-level histograms. IEEE Trans. Syst. Man Cybern. 9 (1), 62–66.

Parkin, Timothy B., 1987. Soil microsites as a source of denitrification variability. Soil Sci. Am. J. 51 (5), 1194–1199.

Parry, S, Renault, P, Chadoeuf, Joel, Chenu, C, Lensi, Robert, 2000. Particulate organic matter as a source of variation in denitrification in clods of soil. Eur. J. Soil Sci. 51 (2), 271–281.

Parry, S., Renault, P., Chenu, C., Lensi, Robert, 1999. Denitrification in pasture and cropped soil clods as affected by pore space structure. Soil Biol. Biochem. 31 (4), 493–501.

Parton, William J, Hartman, Melannie, Ojima, Dennis, Schimel, David, 1998. DAYCENT and its land surface submodel: description and testing. Glob. Planet. Change 19 (1–4), 35–48.

Philippot, Laurent, Hallin, Sara, Schloter, Michael, 2007. Ecology of denitrifying prokaryotes in agricultural soil. Adv. Agron. 96, 249–305.

Piccoli, Ilaria, Dal Ferro, Nicola, Delmas, Patrice J, Squartini, Andrea, Morari, Francesco, 2019. Contrast-enhanced repacked soil cores as a proxy for soil organic matter spatial arrangement. Soil Res. 57 (6), 535–545.

Rabot, Eva, Lacoste, Marine, Hénault, Catherine, Cousin, Isabelle, 2015. Using X-ray computed tomography to describe the dynamics of nitrous oxide emissions during soil drying. Vadose Zone J. 14 (8), vzj2014–12.

Rappoldt, Cornelis, Crawford, John W., 1999. The distribution of anoxic volume in a fractal model of soil. Geoderma 88 (3–4), 329–347.

Rohe, Lena, Apelt, Bernd, Vogel, Hans-Jörg, Well, Reinhard, Wu, Gi-Mick, Schlüter, Steffen, 2021. Denitrification in soil as a function of oxygen availability at the microscale. Biogeosciences 18 (3), 1185–1201.

Schindelin, Johannes, Arganda-Carreras, Ignacio, Frise, Erwin, Kaynig, Verena, Longair, Mark, Pietzsch, Tobias, Preibisch, Stephan, Rueden, Curtis, Saalfeld, Stephan, Schmid, Benjamin, et al., 2012. Fiji: an open-source platform for biological-image analysis. Nature Methods 9 (7), 676–682.

Schlüter, Steffen, Gil, Eshel, Doniger, Tirza, Applebaum, Itaii, Steinberger, Yosef, 2022a. Abundance and community composition of free-living nematodes as a function of soil structure under different vineyard managements. Appl. Soil Ecol. 170, 104291.

Schlüter, Steffen, Roussety, Tim, Rohe, Lena, Guliyev, Vusal, Blagodatskaya, Evgenia, Reitz, Thomas, 2022b. Land use impact on carbon mineralization is mainly caused by variation of particulate organic matter content rather than of soil structure. SOIL 1–23.

Schlüter, Steffen, Sheppard, Adrian, Brown, Kendra, Wildenschild, Dorthe, 2014. Image processing of multiphase images obtained via X-ray microtomography: a review. Water Resour. Res. 50 (4), 3615–3639.

Schlüter, Steffen, Zawallich, Jan, Vogel, Hans-Jörg, Dörsch, Peter, 2019. Physical constraints for respiration in microbial hotspots in soil and their importance for denitrification. Biogeosciences 16 (18), 3665–3678.

Stocker, Thomas, 2014. Climate Change 2013: The Physical Science Basis: Working Group I Contribution to the Fifth Assessment Report of the Intergovernmental Panel on Climate Change. Cambridge University Press.

Surey, R, Kaiser, K, Schimpf, CM, Mueller, CW, Böttcher, J, Mikutta, R, 2021. Contribution of particulate and mineral-associated organic matter to potential denitrification of agricultural soils. Front. Environ. Sci. 9, 640534.

Vogel, H.J., 1997. Morphological determination of pore connectivity as a function of pore size using serial sections. Eur. J. Soil Sci. 48 (3), 365–377.

Vogel, H.-J., Weller, Ulrich, Schlüter, Steffen, 2010. Quantification of soil structure based on Minkowski functions. Comput. Geosci. 36 (10), 1236–1245.

Zheng, Hongbing, Kim, Kyungmin, Kravchenko, Alexandra, Rivers, Mark, Guber, Andrey, 2020. Testing os staining approach for visualizing soil organic matter patterns in intact samples via X-ray dual-energy tomography scanning. Environ. Sci. Technol. 54 (14), 8980–8989.